Chapter 2

Experimental Setup

In this chapter, the details of the experimental setup are presented. The setup essentially consists of three interchangeable *ion sources* connected to a high vacuum chamber housing a *tandem mass spectrometer*, combinded with a *free electron laser*. The three ion sources are a laser vaporization source, an electrospray source, and an electron impact source. In the tandem mass spectrometer cluster ions are mass selected by quadrupole mass filters before and after infrared photodissociation (IR-PD). IR-PD takes place in the tandem mass spectrometer, inside a radio frequency ion trap, where ions are thermalized to a known temperature by collisions with helium buffer gas and accumulated to reduce source instability and to maximize number density (Section 2.2). IR-PD requires an intense source of tunable, monochromatic, IR light (see Section 1.3.4). Such requirements are met by the "Free Electron Laser for Infrared eXperiments" (FELIX) at the FOM Institute for Plasma Physics Rijnhuizen (Nieuwegein, The Netherlands), that was used for all the here presented experiments (Section 2.3). Some basic principles of ion optics related to radio frequency ion traps are presented (Section 2.4) at the end of this chapter.
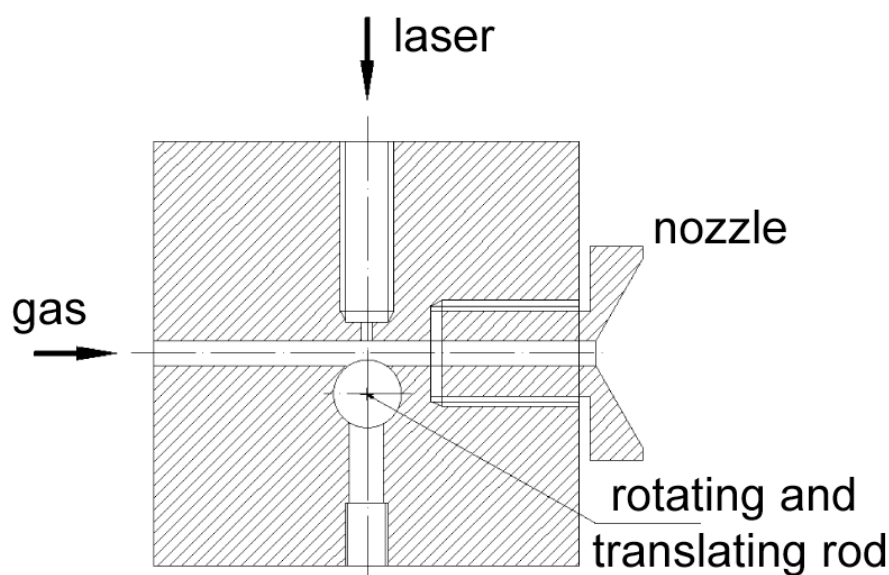
2.1 Ion Sources

2.1.1 Laser Vaporization Source

This source is essentially derived from the source used by Smalley in the discovery of Fullerenes [57]. A few nanosecond long laser pulse (typically in the visible spectral range) impinges on a metallic target and the metal vapor produced by the early portion of the laser pulse forms a dense cloud near the metal surface. This cloud is then quickly ionized and the resulting plasma absorbs light, so that the metal surface is shielded from further ablation. Too much power, i.e., too many photons following the ones that are necessary to create the plasma, is not desirable because it only leads to

super-heating of the plasma. Nanosecond pulses are generally preferred above longer pulses (microsecond range) because the dominant material removal mechanism under these long pulses turns out to be ejection of liquid droplets entrained in the expanding vapor. These droplets play the unfavorable role of condensation nuclei, preventing the production of highly super-saturated metal atom vapor. The plasma is mixed with inert buffer gas flowing in synchronous pulses and the excess heat is transferred by the buffer gas to the cavity walls. As the vapor cools in the carrier gas, clustering begins to occur [58–60]. The jet can be allowed to expand freely, immediately after the plasma-region; yet in order to achieve a better thermalization, either a channel (2–3 cm) or some pre-expansion room is often used. In order to reduce the deposition of material on the walls, a bigger cavity for the plasma-region where the vaporization takes place can be introduced before the channel [61,62]. It has to be noted that the clustering of metal atoms requires three-body collision processes, so the rate of formation of metal clusters falls off quickly as soon as the gas begins to expand freely. Thus, clusters are predominantly formed before exiting the channel where the buffer gas density is sufficiently high to thermalize the metal vapor to near room temperature. The final temperature of the clusters is determined by the number of collisions with the "cold" buffer gas in the source (controlled by pressure and residence time), and the supersonic expansion (determined by pressure difference and nozzle configuration). Note, the two mechanisms used for controlling the temperature couple differently to vibrational, translational, and rotational modes of clusters. While one can expect equal partitioning of energy over all the different degrees of freedom in the source, supersonic expansion is efficient only in cooling translations and rotations, while the vibrational temperature remains close to the source temperature [63].
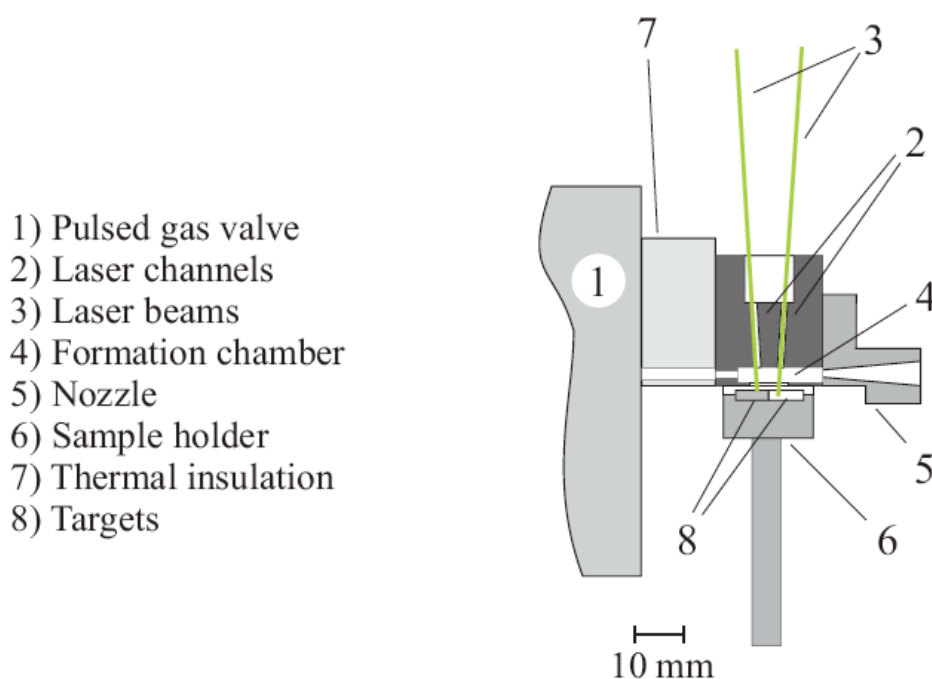
Single Target Laser Vaporization Source   A drawing of the single target variant of the laser vaporization source is shown in Figure 2.1. Vaporization is induced by the second harmonic (532 nm) of a flash lamp pumped Quantel Nd:YAG laser, model CFR 200, which produces 8 ns pulses at a repetition rate up to 100 Hz. Typical laser energies used for this source are ∼10 mJ per pulse. The beam is focused by means of a 150 mm lens on the surface of the metal target. In order to prevent the laser from drilling deep irregular holes in the metal, the target is designed in form of a rod which is rotated and translated by a mechanical connection to a motor driven screw-thread system. This solution provides a good pulse-to-pulse reproducibility. Very broad distributions of clusters can be produced in the whole range spanned by the quadrupoles (1–1000 Dalton) with different gas mixtures. For vanadium oxide clusters, for example, mixtures of about 1% oxygen in helium are found to be optimal for clusters V_nO_m, with $10 < n + m < 30$ and $n < m$. Slightly higher or lower oxygen concentrations can be used to enhance the production of higher or lower oxidized species, respectively. The gas pulses are generated by a standard pulsed valve (General

Figure 2.1: Section of the main body assembly of the single target laser vaporization source.

Valve Company) with a backing gas pressure of 2 to 5 bar.

Dual Target Laser Vaporization Source   The dual-target dual-laser source provides a high flexibility in producing bimetallic oxides. This source was developed in the Katholieke Universiteit Leuven (Leuven, Belgium), in the group of Peter Lievens [64]. Briefly, intense gas pulses are generated by a pulsed supersonic valve (PSV, R. M. Jordan Co.) For the present experiments, the PSV generates 150 µs long pulses at 10 Hz repetition rate with gas inlet pressures of about 5 bar. A drawing of the Leuven cluster source is given in Figure 2.2. The source is thermally insulated from the pulsed gas valve by a 15 mm teflon block, through which a channel of 3 mm diameter is drilled. Inside the source body, made from a stainless steel block, there are three crossing channels. A long lengthwise channel, the formation chamber (17 mm long, 3 mm diameter), is terminated on one side by the gas valve, on the other side by a detachable nozzle. Helium gas is released in this channel and expands through the nozzle into the vacuum system. Inside the formation chamber, the nucleation process takes place. Perpendicular to the formation chamber, two laser channels (1 mm diameter) are tapered. Two independent laser beams, whose firing time, spot size, and pulse energy can be controlled separately, are aligned through these laser channels. The second harmonic of two Nd:YAG lasers (two Quanta Ray GCR Series by Spectra Physics) are used as vaporization lasers. The channels are close to each other to allow simultaneous evaporation of the two metals. In this fashion, heterogeneous clusters

1) Pulsed gas valve
2) Laser channels
3) Laser beams
4) Formation chamber
5) Nozzle
6) Sample holder
7) Thermal insulation
8) Targets

10 mm

Figure 2.2: Schematic representation of the dual-target dual-laser vaporization source. [64]

can be produced. The laser channels are terminated on one side by the two rectangular (7.5 x 25 mm² each) targets. The other side is covered with a glass plate, to avoid the escape of helium gas and metal particles through the laser channels.

The metal targets are mounted in a brass target holder, which is pressed against a slit in the formation chamber. A teflon seal prevents gas leaks. Hole drilling in the target by the vaporization lasers is avoided by moving the target holder. A home-built translation system shifts the targets along a closed loop pattern. This way, the laser pulses scan the entire sample surface and long-term stable cluster production is achieved [65].

2.1.2 Electrospray Source

The electrospray technique was first proposed by Malcolm Dole in 1968 [66], in order to produce molecular beams of large ions. The essence of Dole's idea was to take advantage of what happens during the evaporation of solvent from a droplet that has a net electric charge. In 1882 Lord Rayleigh had analyzed the behavior to be expected of such a droplet and found that as the solvent evaporated the density of charges on the droplet surface would increase to a critical value, now known as the "Rayleigh Limit", at which Coulomb repulsion would overcome surface tension. He showed that a droplet of radius a_0, surface tension σ, and charge Q, remains stable as long as the

fissility $X = Q^2/(64\pi^2\varepsilon_0\sigma a_0^3)$ does not exceed unity [67]. The resulting instability would cause the droplet to break up into a plurality of offspring droplets.

In 1917 John Zeleny made the first reported observation of this Rayleigh instability in experimental studies on the production and behavior of charged droplets [68]. He passed a stream of conducting volatile liquid through a hypodermic needle tubing maintained at a high potential relative to an opposing counter electrode. The resulting intense electric field at the tube tip dispersed the emerging liquid into a fine spray of charged droplets. Zeleny was able to see the break-up of charged droplets as solvent evaporated, just as Rayleigh had predicted.

The liquid emerging at a tube exit forms a conical meniscus known as a "Taylor Cone". Its formation was predicted in 1964 by Geoffrey Taylor [69]. As the result of another kind of instability the interaction between viscosity and surface tension produces so-called "varicose waves" on the surface of such a liquid jet [70]. Those waves grow in amplitude until they truncate the jet into a series of uniform droplets. In the electrospray case, the droplets all have excess charges of the same sign, depending on the polarity of the applied field. Coulomb repulsion thus results in a divergence of their trajectories to form a conical "electrospray" of charged droplets.

Dole assumed that the offspring droplets resulting from a Rayleigh instability would continue to evaporate until they too would reach the Rayleigh limit and break up into still smaller droplets. If the original solution were sufficiently dilute, a succession of such Rayleigh instabilities would ultimately produce droplets so small, that each one would contain only one solute molecule. That lone molecule would retain some of its droplet's charge to become a free gas phase ion after the last of the solvent evaporated. In the 1968 paper that described this scenario, Dole also presented preliminary experimental results obtained in an attempt to bring his idea to practice. Yet the mass spectrometers then available were unable to filter singly charged ions with masses larger than about ten thousand Daltons—the macro-ions Dole was interested in. In the 70's John Fenn started to study electrospray ionization using smaller ions. He then improved the mass spectrometers until he could process molecules as heavy as several million Daltons and was able to produce intact ions in the gas phase of at least 5,000,000 Daltons. Fenn received the Nobel prize for chemistry in 2002 "for his development of soft desorption ionization methods for mass spectrometric analysis of biological macromolecules" [71].

The microscopical model suggested by Dole—known as *Charged Residue Model* (CRM)—to account for the formation of free ions from liquid droplets turned out to be unable to explain the results accumulated by Fenn and coworkers. In particular, it is difficult to conceive how the sequence of Rayleigh instabilities could produce, for each of several species in the same solution, singly charged ultimate droplets containing only one molecule of that species. Moreover, if CRM is to explain the results, the relative number of those droplets for each species would have to be in direct proportion to the relative concentration of that species [71, 72]. How could the droplet know how

to program its sequence of Rayleigh instabilities to produce a distribution of ultimate droplets, such that the number of those ultimate droplets containing one molecule of any species x is always directly proportional to the concentration of species x in the original solution? This would happen, if the droplet subdivision continued until all the droplets contained only one solute molecule. In this case, the subdivision process should produce ultimate droplets for each ionizable species in a solution. One should then always find a spectral peak for every species in such a solution and that was not the case for Fenn's results. An alternative and somehow more convincing model was proposed by J. Iribarne and B. Thomson [73–75], the *Ion Evaporation Mechanism* (IEM). They also assume that a sequence of evaporation steps followed by Rayleigh instabilities leads to smaller and smaller droplets. The IEM postulates that before the droplets become small enough to contain only one solute molecule, the field strength at the droplet surface becomes intense enough to "lift" a surface ion from the droplet into the ambient. In other words, the surface field can evaporate an ion from the droplet surface. Summarizing with John Fenn's words: "There is no unanimity in the electrospray community as to which model is correct. The feeling in this corner is that under most circumstances the IEM is more consistent with more experimental observations than the CRM. However, sometimes the CRM seems more likely to apply, especially in the case of very large molecules" [71].
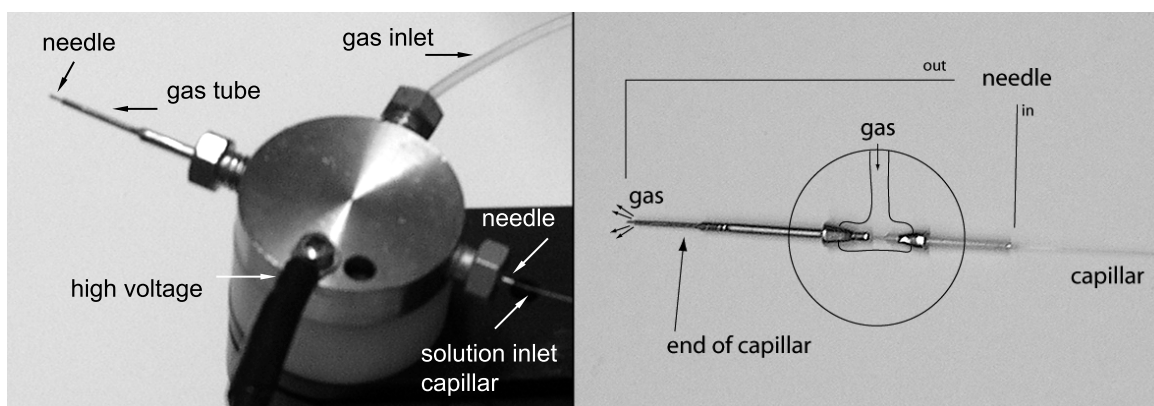
Figure 2.3: Left: a picture of the electrospray source. Right: the central steel disc has been removed and needle, gas tube, and capillary tube can be seen. See text for details.

The electrospray source used in the present experiments is taken from a commercial SCIEX API III triple quadrupole mass spectrometer and adapted to the tandem mass spectrometer. Some details are shown in Figure 2.3. The solution is pumped in a fused silica *capillary tube* with inner diameter of 50 μm. The capillary tube is inserted in a stainless steel *needle* that crosses the electrospray assembly. The solution emerging from the tip of the needle forms the Taylor cone, from which droplets are then ejected.

The part of the needle close to the electrospray ejection is inserted in a metallic tube, called *gas tube.* Needle, capillary, and gas tube are inserted in a steel disc that holds them in place and is mounted on a translation and rotation stage, so that the electrospray can be arbitrarily oriented. A plastic tube, which carries the nebulizer gas, is plugged in the side of the disc. The gas expands in a hollow space inside the disc and flows in the gas tube around the needle. All other junctions are sealed (see the right part of Figure 2.3). The disc, and consequently all other metallic parts—in particular the needle—are electrically connected to a high voltage power supply. The whole electrospray assembly is placed in a chamber at room pressure and temperature. Ions are fed into vacuum through a 75 μm orifice, on which a potential of some tens of volts is applied. The orifice is held in place by a metallic disc, insulated from the orifice and also connected to a voltage power supply.

2.1.3   Electron-Impact Source

The crossed electron beam source consists of a continuous expansion, which is crossed by a continuous beam of 1 kV electrons from an electron gun. The electron gun has been adapted from a cathode ray tube of a Tektronik oscilloscope, where the electrons are thermionic emitted by a thorium-coated iridium filament.[1] The gas expansion contains a certain amount (typically on the order of 1%) of the precursor of the species of interest seeded in helium or argon. This gas mixture expands from a pressure of about 8 bar into vacuum (pressure below 10^{-3} mbar) through a 10–100 μm orifice. At 8 bar the mean free path of helium atoms is in the order of hundredths of microns. Therefore, the *Knudsen number* is much smaller than one and the expansion is supersonic.[2] Cations are easily created by collisions with fast electrons. Secondary, slower, electrons extracted from the carrier gas can be temporarily captured by neutral molecules or clusters forming short-living anions. These species are either stabilized by three body collisions or decay via electron emission or dissociative attachment forming a stable negative ion and a neutral species. Stable species are cooled in the supersonic expansion and may further react with other neutral molecules in the gas jet.

For experiments on the hydrated electron (see Chapter 8), a Even-Lavie pulsed valve [77] was borrowed from the Daniel Neumark's group (University of California, Berkeley, U.S.A.). Cluster ion production occurs according to the same principle as with the continuous expansion, except for the characteristics of the expansion. The Even-Lavie valve produces very short gas pulses (about 30 μs), allowing for very

---

[1]For a detailed description of the electric circuit concerning the electron-gun power supply, see C. Kaposta [76].

[2]*Knudsen number* is defined as the ratio between the mean free path λ and the diameter of the gas container d, which in this case is the diameter of the orifice, the place where the expansion starts (see also page 28).

efficient expansion conditions and, consequently, for efficient clustering and cooling.

2.2 Tandem Mass Spectrometer

A scheme of the instrument is shown in Figure 2.4. The cluster ions are formed in the ion source region (not shown in the picture). The beam of ions passes through a 2 mm diameter skimmer and charged cluster are focused into a radio frequency (RF) decapole ion guide (see Section 2.4), filled with He or Ar buffer gas—depending on the size of the clusters of interest. Many collisions with the buffer gas inside the RF decapole compress the velocity distribution of the ions and thermalize the internal degrees of freedom of the ions to room temperature. The thermalized ions are deflected by an electrostatic quadrupole deflector over 90° and then enter the first quadrupole mass filter (Q1). After a second 90° deflection, ions are focused by a set of two Einzel lenses into a cooled, He-filled, RF hexadecapole ion trap. The ion trap is housed in a cylindrical vessel of gold-plated copper. The trap housing is directly connected to the head of a closed-cycle He-cryostat and kept at a temperature of ∼17 K. Ions in the trap are thermalized to ambient temperature by inelastic collisions with the He buffer gas. The trap is longitudinally crossed by FELIX light pulses. Ions can be trapped, stored, and released by changing the potentials of the entrance and exit lenses of the ion trap.
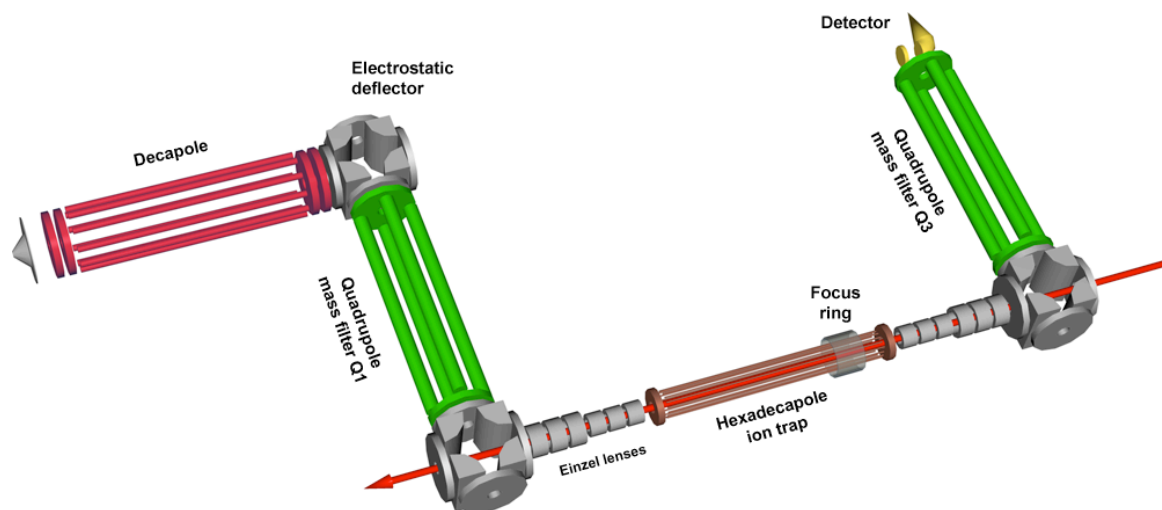
Figure 2.4: Schematic 3D-representation of the guided ion beam tandem mass spectrometer.

Another set of two Einzel lenses reshapes the ion beam after the extraction from the ion trap and guides the ions to a third 90° electrostatic quadrupole deflector. The

ions are then mass-selected by a second RF quadrupole mass filter (Q3) and finally detected by a Channeltron (model CEM 4873 by Burle Industries, Inc.).

Coupling between the Tandem Mass Spectrometer and FELIX

The placement of the trap between two 90° electrostatic quadrupole deflectors allows for an easy alignment of the laser through the trap. FELIX is coupled to the machine—parallel to the trap axis—through a coated ZnSe window and a KBr window, and its light is focused into the trap by a 48 cm focal length KBr lens. Typically, FELIX is used with a bandwidth about 0.3% of the central wavelength and ∼50 mJ per macropulse, measured before the ZnSe and KBr optics. The transmission efficiency of the KBr optics is ≥85% between 3 and 20 μm, while the efficiency of the coated ZnSe window is ≥85% between 8 and 15 μm and about 50% at 6 and 17 μm. For some experiments a KRS-5 window is used instead of the ZnSe window. Its transmission (70–75%) is smaller than that of ZnSe, but considerably less dependent on the wavelength in the region studied here. The overall transmission of these two setups is shown in Figure 2.5 as a function of photon energy. When the FELIX wavelength is resonant with a vibrational mode of the trapped anions, multiple photon absorption and dissociation can occur, producing ionic photofragments, as described in equation (1.7). For a measurement cycle, the trap is typically filled (entrance lens: open; exit lens: closed) for 250 ms and ions are then stored for 150 ms (both lenses: closed). During this time, FELIX fires two macropulses, Immediately after the second macropulse the trap is emptied for 200 ms (entrance lens: closed; exit lens: open). The ion yield is recorded as a function of the FEL wavelength. This data acquisition cycle is repeated multiple times for every wavelength step, depending on the signal intensity. In order to check the stability of the parent ion production, the parent ion yield is measured once at the beginning and once at the end of each wavelength step.

Vacuum and Gas Pressure Measurements

Five cold cathode pressure gauges (Pfeiffer) monitor the pressure in the machine. The first gauge is in the source region, where work is typically carried out at pressures between 10^{-6} mbar (with the 10 Hz laser vaporization source) and 10^{-3} mbar (with the electro-spray). The second gauge is close to the decapole ion guide, the third at Q1, the fourth at the ion trap, and the fifth at Q3. Every region is differentially pumped: the source is pumped by a 1600 l/s turbomolecular pump (TMP), all other four regions by four 500 l/s TMP (Pfeiffer). The background pressure (all gas inlets closed) is 10^{-7} mbar in the source and 10^{-8} mbar in the rest of the machine.

The pressure inside the trap is an important parameter in order to know the exact experimental conditions as well as for daily retrieving of good trapping efficiency.
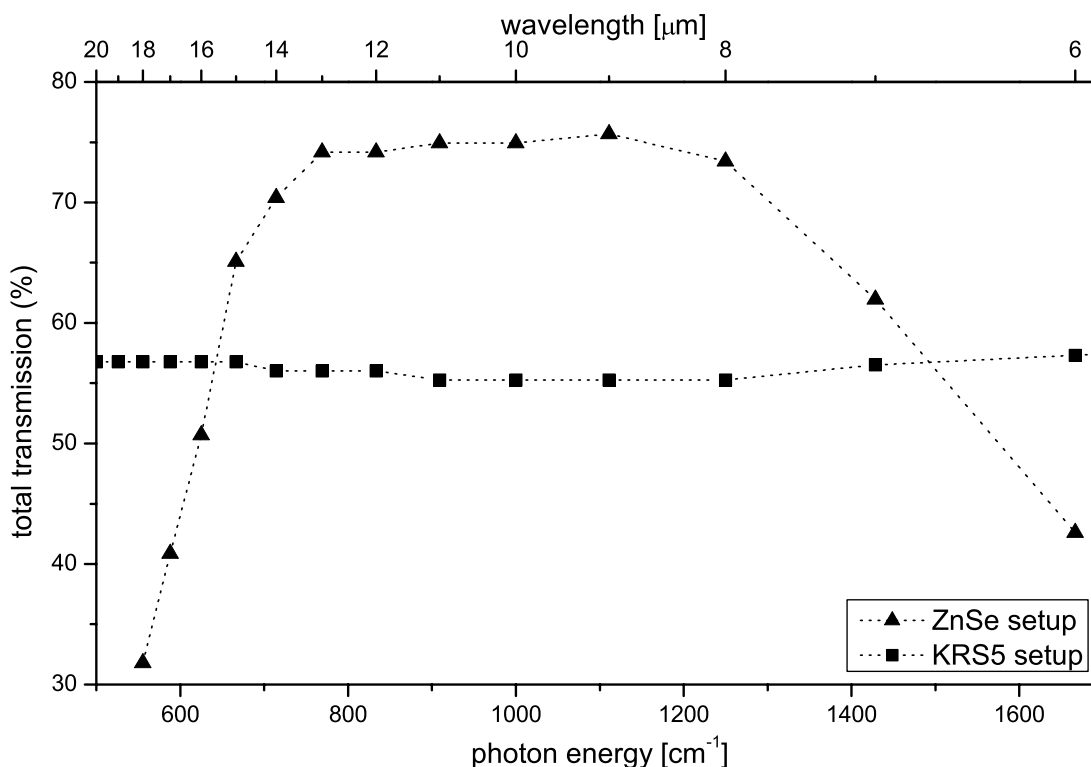
Figure 2.5: Total transmission of the optical path for the two setups, ZnSe and KRS5 (see text), measured by a Fourier transform infrared spectrometer.

Helium buffer gas is introduced directly into the trap housing by a tube twisted around the cold finger of the cryostat and inserted into the trap housing. A similar tube (20 cm long with ~1 mm inside diameter) connects the interior of the trap housing to a capacitance manometer (MKS Baratron, Type 627B). The pressure measurement is based on the capacitive measurement of the deformation of a membrane which is accurately kept at 318 K.

It has to be noticed that the behavior of gas molecules is ruled by a pressure gradient in a viscous regime and by diffusion in a molecular regime. The two regimes are discriminated by the ratio between the mean free path λ and the "diameter" d of the vacuum system. The parameter λ/d is known as *Knudsen number*. If $\lambda/d \ll 1$ the flow is viscous; if $\lambda/d > 1$ the flow is molecular. This can be rationalized considering that in a viscous regime, the interaction of the gas molecules with each other is dominant, whereas it can be neglected in the molecular regime. It is then clear that in the viscous regime under equilibrium conditions, the pressures at the two openings of the tube (trap and Baratron sides) must be equal independent of the temperature, otherwise the motion of the gas molecules will follow the pressure gradient. In the molecular regime, the pressure does not have to be homogeneous. If different regions

are held at different temperatures one will necessarily obtain different values for the pressure.

Since the trap can be cooled down to 17 K while the manometer is constantly kept at 318 K, it is worth analyzing this situation in detail. Let us first assume a situation in the molecular regime. The active membrane exposed to the pressure to be measured is assumed to be in thermal equilibrium with the gas in its neighborhood. However, inside the tube connecting the trap with the Baratron there is a temperature gradient. This situation can be simplified assuming an ideal surface separating two regions, each at a different temperature (T_{low} and T_{high}). The diffusion rate across an ideal surface is proportional to the number of molecules n and to their velocity component in the direction perpendicular to the surface, $v_\perp$. If a molecule has an energy of $k_{\text{Boltz}}T/2 = mv^2/2$ for every translational degree of freedom, it will have a velocity component $v_\perp$ of $\sqrt{k_{\text{Boltz}}T/m}$ (where m is the mass of the molecule). Therefore the diffusion rate across the surface will be proportional to the number of molecules n and to $\sqrt{T/m}$. Under equilibrium conditions, an equal number of molecules must cross this ideal surface in both directions in a time unit. One obtains

$$n_{\text{low}}\sqrt{\frac{T_{\text{low}}}{m}} = n_{\text{high}}\sqrt{\frac{T_{\text{high}}}{m}}$$

or,

$$\frac{n_{\text{low}}}{n_{\text{high}}} = \sqrt{\frac{T_{\text{high}}}{T_{\text{low}}}}.$$

Using $PV = nk_{\text{Boltz}}T$ and considering the same volume on both sides of the ideal surface, one obtains

$$\frac{P_{\text{low}}}{P_{\text{high}}} = \frac{n_{\text{low}}T_{\text{low}}}{n_{\text{high}}T_{\text{high}}} = \sqrt{\frac{T_{\text{high}}}{T_{\text{low}}}}\frac{T_{\text{low}}}{T_{\text{high}}} = \sqrt{\frac{T_{\text{low}}}{T_{\text{high}}}}$$

and it can be concluded that

$$P_{\text{low}} = P_{\text{high}}\sqrt{\frac{T_{\text{low}}}{T_{\text{high}}}}.$$

Repeating this for every possible surface along the temperature gradient, so that for example

$$P_{\text{lower}} = P_{\text{low}}\sqrt{\frac{T_{\text{lower}}}{T_{\text{low}}}} = P_{\text{high}}\sqrt{\frac{T_{\text{low}}}{T_{\text{high}}}}\sqrt{\frac{T_{\text{lower}}}{T_{\text{low}}}} = P_{\text{high}}\sqrt{\frac{T_{\text{lower}}}{T_{\text{high}}}}$$

it can be concluded that the only important parameters are the temperatures at the two sides of the tube, obtaining

$$P_{\text{trap}} = P_{\text{measured}}\sqrt{\frac{T_{\text{trap}}}{T_{\text{Baratron}}}} \quad . \tag{2.1}$$

The reading has therefore to be corrected by a factor proportional to $\sqrt{T_{\text{trap}}}$.

Conversely, assuming the conditions for a viscous regime, the Baratron reading should not be corrected. To address this question, one can calculate the mean free path for helium atoms, which are by far the most abundant species in the trap. Typically, good trapping conditions are achieved for a Baratron reading of 0.02 mbar at 17 K. According to equation (2.1), it corresponds to a pressure of 0.005 mbar. The mean free path can now be calculated according to

$$\lambda = \frac{k_{\text{Boltz}} T_{\text{trap}}}{\sqrt{2}\pi d^2 P} \tag{2.2}$$

where d is the diameter of a helium atom[3] and P the pressure. It is found that $\lambda \geq 1$ mm both assuming a pressure of 0.02 mbar (Baratron reading not corrected) or of 0.005 mbar (corrected) (see Figure 2.6). Therefore, the pure viscous regime
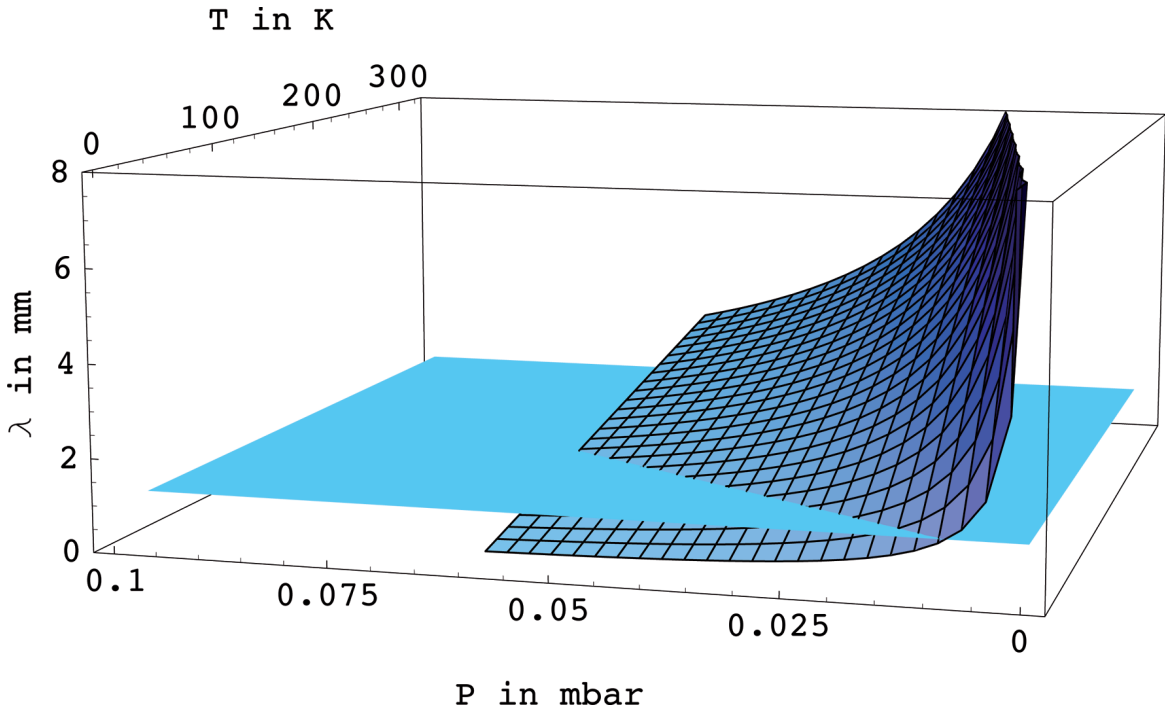
Figure 2.6: A plot for the mean free path in dependence on the temperature and the pressure. The plot is cut by a plane at $\lambda = 1$ mm.

has to be excluded. However, one can argue that the experimental conditions are close to a transition regime between molecular and viscous flow. In order to clarify the regime at hand, the Baratron readings for different gas flows (using a MKS flow

---

[3]The diameter of a helium atom is assumed to be 2.58Å. according to ref. [78].

meter) and at different temperatures (100, 200, and 300 K) are recorded. To evaluate this measurement, one has to consider the gas flowing out of the trap, through the entrance and exit lenses that have a 1 cm diameter hole.

Molecular regime: The gas leaves the trap due to diffusion with a rate proportional to the square root of the temperature ($\rho \propto 1/\sqrt{T_{\text{trap}}}$). Therefore, the pressure has to increase proportionally to the square root of the temperature ($P_{\text{trap}} \propto T_{\text{trap}}/\sqrt{T_{\text{trap}}} = \sqrt{T_{\text{trap}}}$). Since the Baratron reading has to be corrected by a factor $\sqrt{T_{\text{trap}}}$, the same readings are expected for all temperatures, which will only correspond to the correct pressure at 318 K.

Viscous regime: The gas leaves the trap due to the pressure gradient. Since the pressure outside the trap is three order of magnitude lower than inside, one can assume that the gradient remains constant independent of the temperature, which spans only a factor three in the inspection of the pressure readings. Therefore, the pressure inside the trap must remain constant. In this case, the Baratron reading does not have to be corrected. The same readings are expected for all temperatures.

Transition regimes: This is the only case in which the Baratron readings are expected to be different at varying temperatures for the same gas flow. In fact, for the molecular scenario, there are two diffusion processes: one through the tube to the manometer and one through the entrance and exit lenses, where the two apertures have different diameters of 1 mm and 1 cm, respectively. Therefore the flow into the tube is expected to become diffusive at shorter mean free path lengths (lower temperatures) than the flow through the lenses. In this case, Baratron readings need to be corrected (at least partially), whereas the gas flow from the trap is virtually temperature independent.

From the measurements shown in Figure 2.7, no significant dependence on the temperature can be observed. It can therefore be concluded that the experimental conditions are in the molecular regime and the Baratron reading must be corrected according to equation (2.1).

A typical helium working pressure in the ion trap is 5–$7{\cdot}10^{-3}$ mbar—whereby the pressure reading outside the trap taken with the cold cathode pressure gauge is about 10^{-5} mbar. Under these conditions the mean free path of the ions in the trap at 17 K can be estimated to be in the order of tens to hundreds of micrometer, according to equation (2.2), and the mean time between ion-helium collisions to be in the order of microseconds.

Furthermore, the decapole is housed in a stainless steel cylinder and the pressure is measured in the vacuum chamber close to this housing. The pressure in the decapole
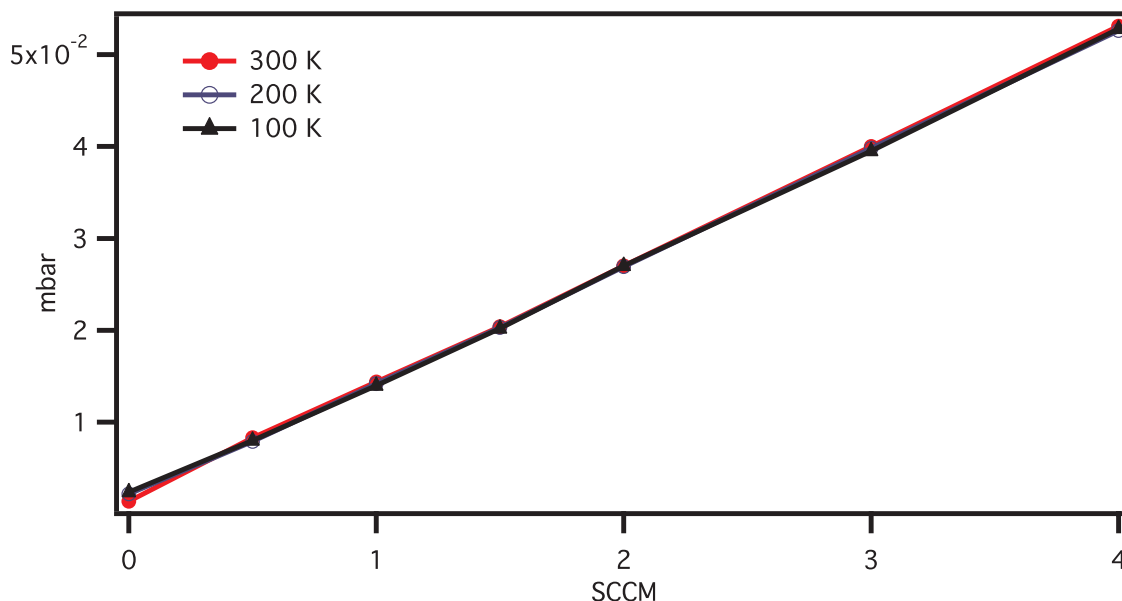
Figure 2.7: Baratron readings (in mbar) in dependence on the gas flow to the trap (in Standard Cubic CentiMeters), measured at 100, 200, and 300 K.

cannot be measured directly. Nevertheless, a rough estimate can be given by comparing the pressure around the decapole with the one around the hexadecapole ion trap. The reading on the cold cathode at the decapole under typical working conditions is $5 \cdot 10^{-5}$ to $1 \cdot 10^{-4}$ mbar, therefore a factor five to ten higher than at the ion trap, while the temperature is about 10–15 times higher. Thus, the mean free path in the decapole is assumed to be similar or slightly larger that the one in the ion trap.

2.3 Free Electron Laser for Infrared eXperiments (FELIX)

2.3.1 Principle of Free Electron Laser Operation

The free electron laser (FEL) is a special member of the laser family, in which coherent radiation is produced as a result of oscillations of *free* electrons, instead of electrons that are bound in atoms, molecules, or crystals [79]. The principle of operation is sketched in Figure 2.8. Relativistic electrons are injected into a periodic magnetic structure (of period λ_u), the so-called undulator. It is assumed that the electrons move along the x-axis with speed u and their motion will be treated from the *electron frame* coordinate system. Note that the *electron frame* is not the frame moving with the electrons (where the electrons would have no acceleration and therefore would

emit no light). Instead, it is the inertial frame moving along the x-axis with the same instantaneous speed u as the light-emitting electron. Furthermore, the standard relativistic factors $\beta = u/c$ and $\gamma = 1/\sqrt{1-\beta^2}$ will be used. Since $\gamma = mc^2/m_0c^2$, it is therefore the energy of the light emitting electron (the accelerator energy) expressed in units of m_0c^2, the electron rest energy. The undulator magnet array is now considered as "seen" by the moving electron in the electron frame. The relativistic (Lorentz) frame transformation rules show one important point: the electron "sees" not only an oscillating magnetic field but also an oscillating electric field in the perpendicular direction—in short, it "sees" an *electromagnetic wave*. Its wavelength in the electron frame, λ_u/γ, equals the undulator period λ_u after Lorentz contraction by the γ-factor.[4]
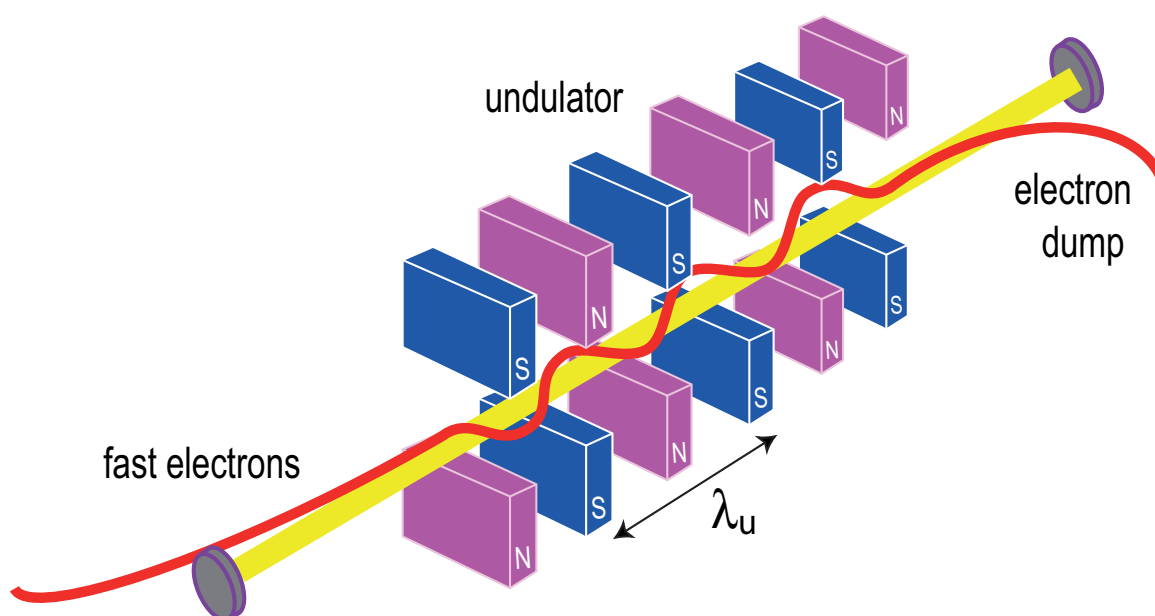
Figure 2.8: Diagram showing the basic ingredients of a free-electron laser: a beam of relativistic electrons, an undulator (with period λ_u) in which the electrons perform a transverse oscillation and emit radiation, and two mirrors forming an optical resonator in which the radiation is amplified by stimulated emission.

Upon interaction with the *electromagnetic wave*, the electron emits (first-harmonic) light of the same wavelength λ_u/γ. Specifically, this is the electron-frame wavelength. The corresponding wavelength in the laboratory frame is subject to the Doppler effect. Along the x-axis, the multiplying Doppler factor is[5] $\sqrt{1-\beta}/\sqrt{1+\beta} \approx 1/2\gamma$. Thus,

---

[4]Example: An undulator period of 65 mm is seen by 40 MeV electrons as a 0.8 mm period.

[5]$\frac{\sqrt{1-\beta}}{\sqrt{1+\beta}} = \frac{\sqrt{1-\beta}}{\sqrt{1+\beta}}\frac{\sqrt{1+\beta}}{\sqrt{1+\beta}} = \frac{\sqrt{1-\beta^2}}{1+\beta} = \frac{1}{\gamma(1+\beta)} \approx \dots \quad$ for $\beta \approx 1 \quad \dots \approx \frac{1}{2\gamma}$

the emitted first-harmonic wavelength along the x-axis in the laboratory frame is[6]:

$$\lambda_0 = \frac{\lambda_u}{\gamma}\,\frac{1}{2\gamma} = \frac{\lambda_u}{2\gamma^2}\,. \tag{2.3}$$

The undulations of the electron with respect to the undulator x-axis decrease its average velocity x-component and therefore, the effective β- and γ-value in the x-direction. The average magnitude of the y-axis component of the velocity is proportional to the acceleration and therefore, to the undulator magnetic field magnitude B. This implies that γ^2 must be replaced by $\gamma^2/(1+K^2)$, where K is a dimensionless parameter proportional to B. Equation (2.3) then becomes

$$\lambda_0 = \frac{\lambda_u}{2\gamma^2}(1+K^2)\,. \tag{2.4}$$

In an oscillator configuration (see Figure 2.8), this *spontaneous* radiation, which is essentially incoherent, is captured in an optical resonator. The stored field induces newly injected electrons to radiate coherently, which results in the build-up of high laser power. The newly injected electrons will see the superposition of two electromagnetic fields: the one due to undulator and the one due to the light stored in the cavity. In the laboratory frame the electromagnetic wave present in the cavity will have a phase

$$\psi = \Big((k_0 + k_u)x - \omega_0\,t\Big)\,, \tag{2.5}$$

where k_0 and k_u are the wave-vectors associated with light and undulator, respectively; and ω_0 is the angular frequency of light. The propagation velocity of this wave, called ponderomotive wave, is $v_x = \omega_0/(k_0 + k_u)\ (<c)$. Thus, it is possible for the electron to travel at the same velocity as the ponderomotive wave.

In order to understand qualitatively the energy transfer one can use the analogy to a group of surfers attempting to catch a series of waves.[7] In the attempt to match velocities with the waves, some will catch a wave ahead of the crest and slide forward while others will catch a wave behind the crest and slide backwards. As a result, clumps of surfers will collect in the troughs of the waves. Those surfers which slide forward ahead of the wave are accelerated and gain energy at the expense of the wave, while those that slide backward are decelerated and lose energy to the wave. The wave grows if more surfers are decelerated than accelerated, and there is a net transfer of energy to the wave. The free-electron laser operates by an analogous process. Electrons in near resonance with the ponderomotive wave lose energy to the wave if

---

[6]Example: 40 MeV electrons in an undulator with a period of 65 mm radiate at 5 μm.

[7]For a detailed analytical description of light amplification in a free electron laser, see, for example, T. C. Marshall [79]. Basic principles of Free Electron Lasers can be found, for example, at: http://www.rijnhuizen.nl/felix and URL's cited there.

their velocity is slightly greater than the phase velocity of the wave, and gain energy at expense of the wave in the opposite case. As a result, wave amplification occurs if the wave lags behind the electron bunch. The ponderomotive phase in equation (2.5) satisfies the circular pendulum equation

$$\frac{\mathrm{d}^2}{\mathrm{d}\,z^2}\psi = -Q^2 \sin\psi\,, \tag{2.6}$$

where the pendulum constant Q is proportional to the square root of the product of the undulator and the radiation fields [79]. There are two classes of trajectories: trapped and untrapped. The untrapped, or free streaming orbits correspond the case in which the pendulum swings through the full 360° cycle. The electrons pass over the crests of many waves, traveling fastest at the bottom of the troughs and slowest at the crests of the ponderomotive wave. In contrast, the electrons are confined within the trough of a single wave in the trapped orbits. This corresponds to the motion of a pendulum which does not rotate the full circle, but is confined to oscillate about the lower equilibrium point. The dynamical process is one in which the pendulum constant evolves during the course of the interaction. Electrons lose energy as the wave is amplified; hence, the electrons decelerate and both the pendulum constant and separatrix grow. Ultimately, the electrons cross the growing separatrix from untrapped to trapped orbits. This ordinate distribution of the electrons on a wavelength scale (known as *micro-bunching*) is responsible for the coherence of the amplified light.

2.3.2   FELIX

At FELIX, an injector consisting of a thermionic triode electron gun, modulated at 1 GHz and followed by a prebuncher and a buncher, produces 3.8-MeV electron pulses. These electrons are further accelerated in two 1-GHz traveling-wave radio frequency linear accelerators (RF linacs) to energies of 15–25 and 25–45 MeV, respectively. Behind each linac, the electron beam can be bent into a FEL (see Figure 2.9). Both FELs have identical undulators consisting of two rows of permanent magnets forming 38 field periods of 65 mm length. The distance between the rows can be varied to change the K-value of the undulator and thereby scan the wavelength of the laser. Two gold-plated copper mirrors placed at opposite sides of the undulator define the resonator. Behind the undulator the electrons are bent out of the resonator and dumped. The larger part of the space between the mirrors is taken up by electron beam bending and focusing magnets, vacuum valves, etc., rather than by the undulator, which leads to a cavity length of 6 m. A fraction of the optical radiation generated in the laser cavity is coupled out through a central hole in one of the end mirrors, collimated by a spherical mirror, and transported through a beam transport system from the accelerator vault to the user stations in the experimental area. [36, 37].
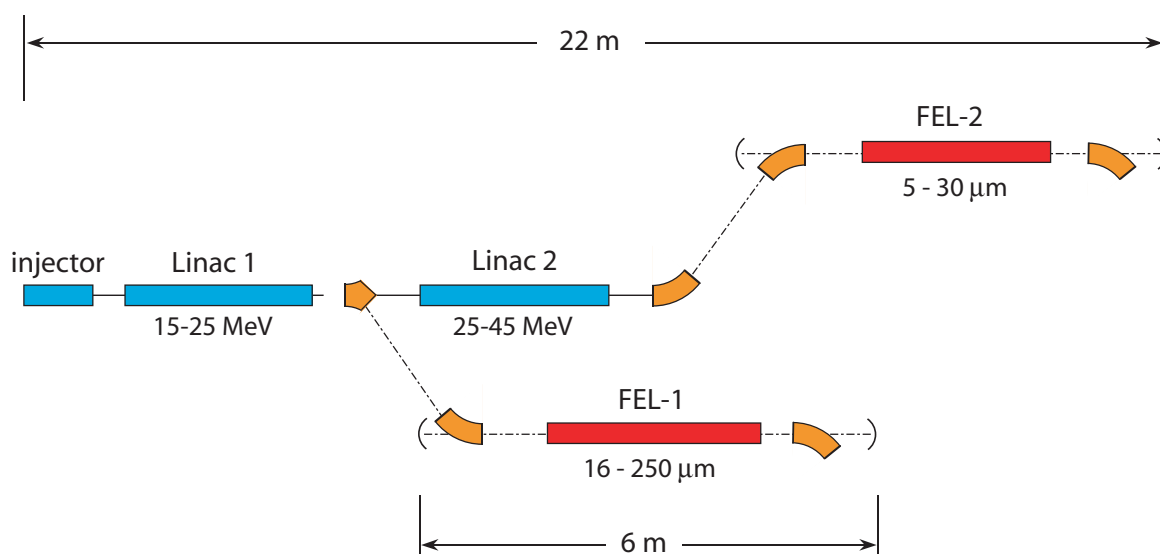
Figure 2.9: Layout of FELIX. The electron beam from Linac1 can be either steered into FEL-1, which is used for the long wavelength range (16–250 μm), or further accelerated in Linac2 and injected into FEL-2 for the shorter wavelength range (5–30 μm).

It is evident that the time structure of the light in a FEL closely mimics the time structure of the electron beam. At FELIX, the power supplies of the linacs allow for a duty cycle up to 10 Hz, where every *macropulse* of electrons can last up to 10 μs. The radio frequency linacs deliver a series of electron *micropulses* with typical GHz repetition rate, within every macropulse. The corresponding time structure of the FELIX laser pulses is depicted in Figure 2.10. 1-ps micropulses are separated by intervals of 1 ns (or 40 ns) and grouped in 5-μs macropulses. The repetition rate of the macropulses is up to 10 Hz. The wavelength range is between 4.5 and 250 μm (2200–40 cm^{-1}) and by using special mirrors it is possible to operate the FEL at the third harmonic and thereby the short wavelength limit is shifted to 2.7 μm (3700 cm^{-1}). The energy per micropulse can be up to 50 μJ, while the energy per macropulse ca be up to 100 mJ.

For experiments on gas phase molecular systems, two key requirements for the light source are (*i*) tunability and (*ii*) high fluence on the microsecond time scale (see Section 1.3.4). As discussed above, the wavelength of a FEL is determined by the electron beam energy and the periodicity and strength of the magnetic field in the undulator. At FELIX, the solution of varying the distance between the two rows of magnets allows for a tunability over more than an octave without realignment of the electron beam optics. For energies in the order of 100 mJ on the microsecond time scale no commercial laser, continuously tunable between 5 and 250 μm, is available.
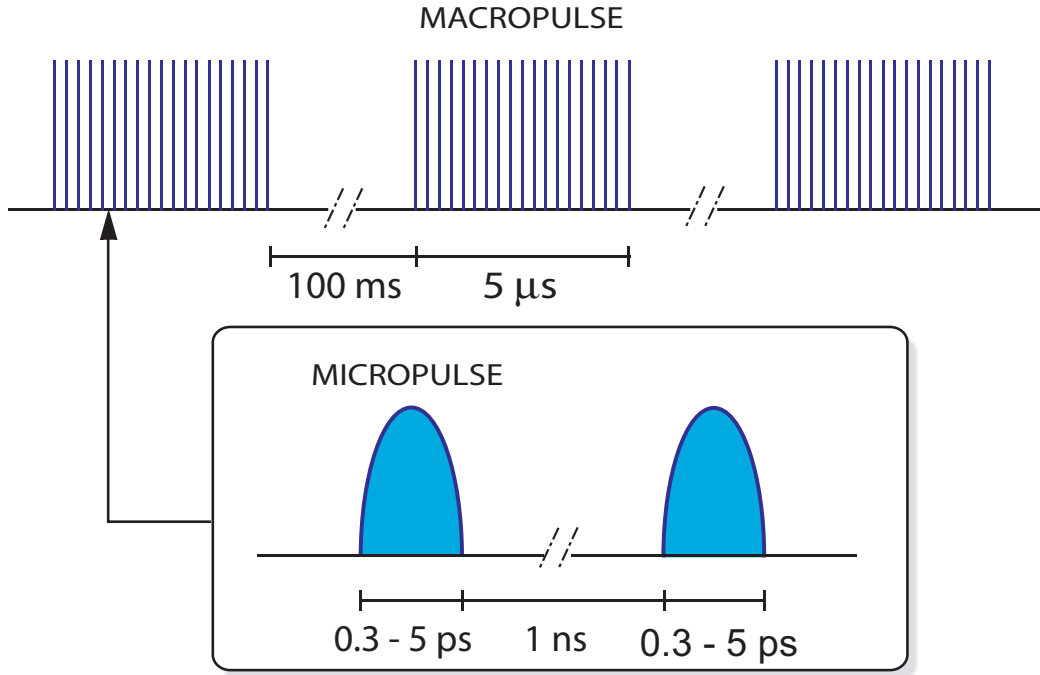
Figure 2.10: The FELIX pulse structure consisting of ∼1-ps *micropulses* separated by 1-ns intervals. Micropulses are grouped in 5-μs *macropulses* separated by 100 ms.

2.4   Ion Optics

The physical properties used to guide, select, and confine ions in the gas phase are their (inertial) mass and charge. Therefore, only electromagnetic fields will be considered.

The differential equation which describes the motion of an ion through a field is obtained from Newton's law of motion

$$\boldsymbol{F} = m\frac{\mathrm{d}^2\boldsymbol{r}}{\mathrm{d}\,t^2}, \tag{2.7}$$

where $\boldsymbol{F}$ is the force on the ion, m is the mass of the ion, and $\boldsymbol{r}$ is the position of the ion. The force on an ion with charge e moving through an electric field $\boldsymbol{E}$ and a magnetic field $\boldsymbol{B}$ with a velocity $\dot{\boldsymbol{r}}$ is given by the Lorentz force law

$$\boldsymbol{F} = e\boldsymbol{E}(\boldsymbol{r}, t) + e\dot{\boldsymbol{r}} \times \boldsymbol{B}(\boldsymbol{r}, t), \tag{2.8}$$

The computation of the $\boldsymbol{E}$ and $\boldsymbol{B}$ fields from the time-varying potential imposed on

the electrodes is performed by employing the Maxwell equations

$$\boldsymbol{\nabla} \cdot \boldsymbol{D} = \rho \qquad\qquad \boldsymbol{\nabla} \times \boldsymbol{E} = - \frac{\partial \boldsymbol{B}}{\partial t}$$

$$\boldsymbol{\nabla} \cdot \boldsymbol{B} = 0 \qquad\qquad \boldsymbol{\nabla} \times \boldsymbol{H} = \boldsymbol{J} + \frac{\partial \boldsymbol{D}}{\partial t}$$

where ρ is the real charge density in the medium and $\boldsymbol{J}$ is the current per unit area in the medium. However, the Maxwell equations can be drastically simplified as follows:

In vacuum, $\boldsymbol{D}$ and $\boldsymbol{E}$ are proportional through the vacuum permittivity ε_0, and $\boldsymbol{B}$ and $\boldsymbol{H}$ are proportional through the vacuum permeability μ_0. Furthermore, the charge density of ions ρ and the associated current density $\boldsymbol{J}$ are assumed to be negligible for the purpose of computing the $\boldsymbol{E}$ and $\boldsymbol{B}$ fields acting on them. The previous assumption is justified for ion densities below $10^7/\mathrm{cm}^3$ [81], and such density is referred to as the *space charge limit*.

Under these assumptions the Maxwell equations can be re-written as,

$$\boldsymbol{\nabla} \cdot \boldsymbol{E} = 0 \qquad\qquad \boldsymbol{\nabla} \times \boldsymbol{E} = - \frac{\partial \boldsymbol{B}}{\partial t}$$

$$\boldsymbol{\nabla} \cdot \boldsymbol{B} = 0 \qquad\qquad \boldsymbol{\nabla} \times \frac{\boldsymbol{B}}{\mu_0} = \frac{\partial (\varepsilon_0 \boldsymbol{E})}{\partial t} \, .$$

If B_0 and E_0 are the maximum amplitudes of the $\boldsymbol{B}$ and $\boldsymbol{E}$ fields, the speed of light is $c = (\varepsilon_0 \mu_0)^{-1/2}$ and $B_0 = E_0/c$ [82]. Thus the $\boldsymbol{B}$ field in the Lorentz force law (2.8) exerts a negligible force on the ion compared to the $\boldsymbol{E}$ field unless the ion is moving at a speed comparable to the speed of light. Therefore, it is not necessary to consider the $\boldsymbol{B}$ fields any further for the purpose of computing the force on an ion. The Lorentz force law (2.8) reduces to

$$\boldsymbol{F} = e\boldsymbol{E} \tag{2.9}$$

while Maxwell's equations become:

$$\boldsymbol{\nabla} \cdot \boldsymbol{E} = 0 \qquad \boldsymbol{\nabla} \times \boldsymbol{E} = 0 \, . \tag{2.10}$$

2.4.1 Multipole Radio Frequency Traps

The problem of confining ions in a determined region can essentially be translated in finding an appropriate three dimensional potential with a well defined minimum. Maxwell's equation

$$\boldsymbol{\nabla} \cdot \boldsymbol{E} = 0 \tag{2.11}$$

becomes Laplace's equation if the electric field is written as the gradient of a potential $\boldsymbol{E} = -\boldsymbol{\nabla}\Phi$,

$$\nabla^2\Phi = 0\,. \tag{2.12}$$

A function Φ which satisfies Laplace's equation is said to be *harmonic*. Gauss's harmonic function theorem says that if a function Φ is harmonic in a sphere, then the value of Φ at the center of the sphere is the arithmetic mean of its values on the surface. Solutions have no local maxima or minima.[8] Because Laplace's equation is linear, superposition of any two solution is also a solution. A solution to Laplace's equation is uniquely determined if the function is specified on all boundaries. Therefore, it is immediately clear that an electrostatic potential, which has to satisfy Laplace's equation and cannot have a minimum in a three dimensional space is not a candidate for a trapping potential.[9]

An Example: The Quadrupole

An electrostatic potential compatible with Laplace's equation is that of a saddle point, for instance:

$$\Phi = \alpha x^2 + \beta y^2 + \gamma z^2 \quad \text{where} \quad \alpha + \beta = -\gamma\,. \tag{2.13}$$

This potential can be simplified assuming it has a constant value along the z-direction. This assumption still allows for a potential compatible with Laplace's equation. In fact, if the potential is constant along the z-direction the constant γ can be set equal to zero in equation (2.13) so that

$$\Phi = \Phi_0\big(\alpha x^2 + \beta y^2\big)\,, \tag{2.14}$$

where Φ_0 is a value independent on any space coordinate. The Laplace's condition (2.12) imposes $\alpha = -\beta$ and since any multiplicative factor can be included into Φ_0, one can write $\alpha = -\beta = 1$ and obtains

$$\Phi = \Phi_0\big(x^2 - y^2\big)\,. \tag{2.15}$$

---

[8]Laplace's equation says that the sum of the second partial derivatives must be zero. If $f(x, y, z)$ had a local minimum (maximum) in $\boldsymbol{v}$, then also its restrictions along every single coordinate should have a local minimum (maximum) in $\boldsymbol{v}$. It means that $\frac{\partial^2 f(\boldsymbol{v})}{\partial x^2} > 0$, $\frac{\partial^2 f(\boldsymbol{v})}{\partial y^2} > 0$, and $\frac{\partial^2 f(\boldsymbol{v})}{\partial z^2} > 0$ (or < 0, for a maximum). But it is clear that if all three second partial derivative are positive (negative) their sum cannot be zero. Therefore, solutions of Laplace's equation have no local maxima or minima.

[9]One could come to the same conclusion also using Gauss's law. By requiring a potential minimum one asks for a point P where the electrostatic field is zero and for a surrounding region where the electric field is pointing in direction of P—assuming one wants to trap a positive charge. But if anywhere on any imaginary surface that encloses P the electric field points toward P the surface integral of the normal component is certainly not zero, but rather a negative number. But Gauss's law says that the flux of electric field through any surface is proportional to the total charge inside. So one must conclude that a positive charge can only be stable on top of a negative one, and vice versa. In this way, the ion would not be trapped in vacuum but on the surface of something else—which has to be held in place by some other force [84].

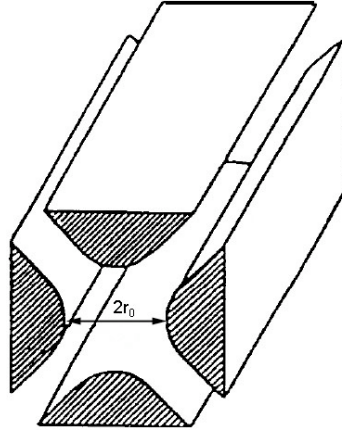This potential, shown in Figure 2.11, is a solution of Laplace's equation and can
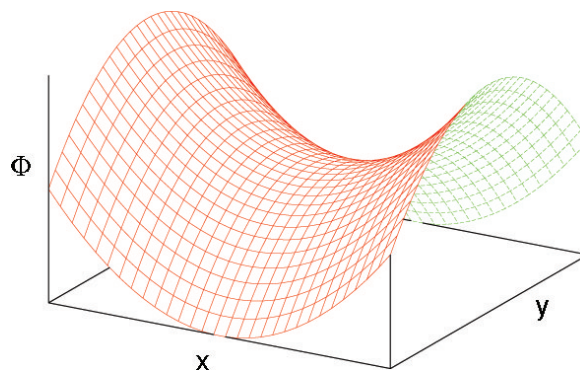
Figure 2.11: The potential $\Phi = \Phi_0\big(x^2 - y^2\big)$.

be generated by fixing its boundary conditions. Since for every equipotential surface Φ', equation (2.15) defines an hyperbola, four hyperbolic metallic (i.e. equipotential) surfaces will be used, extruded in the z-direction like in Figure 2.12. The hyperbolae are set tangent to an inscribed circle with radius r_0 and the opposed electrodes are pairwise connected. By applying a potential difference of $2r_0^2\Phi_0$ between electrode pairs, one obtains the potential (2.15).

It has been already discussed that this saddle potential "imposed" by Laplace's equation is not enough to trap the ions. In fact, while they would oscillate back and forth on the x-direction, their y-coordinate would diverge. This can be avoided if the applied potential difference between electrodes is periodic. Due to the sinusoidal change of the sign of the electric force, focusing and defocusing is obtained in both the x- and y-directions alternating in time, so that the overall effect is a confining potential around the weaker field region.[10]

Now that the ions are confined in the (x, y)-plane, two ring-shaped electrodes can be built at the two sides of the quadrupole. By applying a positive (negative) potential on the two rings, cations (anions) are repelled toward the center of the quadrupole. So the trap is completed. This simple solution for the z-direction confinement can be used in every linear ion trap configuration. Therefore, only on the two-dimensional problem will be discussed in the following paragraphs.

---

[10]Generally, it is true that a charged particle will move toward low field regions if it is subject to a periodic inhomogeneous field. One can intuitively understand it as follows: At a certain point in space and time the particle will be accelerate either toward the stronger field region or toward the weaker one. Suppose the acceleration is toward the weaker field region; the particle flies from stronger to weaker field until it is accelerated in the opposite direction, but this will happen with a weaker force being the particle now in a region of weaker field. If, at the contrary, one starts with an acceleration toward stronger field region, the particle will fly in that direction until a stronger field—and correspondingly a stronger force—will send it back.

Figure 2.12: Four hyperbolic surfaces generate the potential described in equation (2.15) and shown in figure 2.11. [85]

Multipole Solutions

Here, more general solutions will be analyzed, but still within a subset of all the possibilities. In particular, as for the quadrupole case, only infinitely long conductors will be considered whose shape does not vary with z.[11] Although real electrodes structures must necessarily be of finite length, this approximation is made because it captures the essential features for the operation of electric radio frequency devices while avoiding some of the mathematical complexities.

A potential Φ is considered that satisfies Laplace's equation, which can be written as

$$\Phi(x,y) = K_n\, U_n(x,y)\,, \tag{2.16}$$

where K_n is a constant that can be used to adapt the potential to the size of electrodes and to the voltage applied on them. Therefore, one needs only to concentrate on $U_n(x,y)$.

If the complex variable $z = x + iy$ is raised to an integral power n, then the result can be expressed as the sum of two functions, a real $U_n(x,y)$ and an imaginary $V_n(x,y)$ part

$$(x+iy)^n = U_n(x,y) + iV_n(x,y)\,. \tag{2.17}$$

The integer n defines the *order* of the multipole field. From complex variable theory z^n is known to be analytic and so the Cauchy-Riemann equations are applicable [86]:

$$\begin{aligned} \frac{\partial U_n(x,y)}{\partial x} &= \frac{\partial V_n(x,y)}{\partial y} \\ \frac{\partial U_n(x,y)}{\partial y} &= -\frac{\partial V_n(x,y)}{\partial x} \end{aligned} \tag{2.18}$$

---

[11]Therefore, solutions such as ring electrodes traps and Paul traps are ignored.

The sum of the partial derivative of the first of these equations with respect to x and the partial derivative of the second of these equations with respect to y gives

$$\frac{\partial^2 U_n(x,y)}{\partial x^2} + \frac{\partial^2 U_n(x,y)}{\partial y^2} = 0 \, . \tag{2.19}$$

Thus the function $U_n(x,y)$ satisfies Laplace's equation.

The equipotential conductor surfaces are constructed so that they fall on the locus of points in the (x,y) plane defined by $U_n(x,y) = \pm$ constant. The separation between opposite electrodes is chosen to be $2r_0$ to ensure that, for the case of the quadrupole, the standard quadrupole geometry [85, 87] is reproduced (see Figure 2.12).

It has been shown [81] that cylindrical electrodes can well approximate the hyperbolic shapes, reducing significantly the production difficulties. Best results are obtained for cylinders with a diameter d such that

$$r_0 = (n-1)\frac{d}{2} \, . \tag{2.20}$$

Now, the three cases applied in the present experiments are examined:

Quadrupole   Applying the theory of complex variables, the solution for a quadrupole is found as a special case. The function z^n for $n=2$ is evaluated to obtain:

$$\begin{aligned} U_2(x,y) &= x^2 - y^2 \\ V_2(x,y) &= 2xy \, . \end{aligned} \tag{2.21}$$

Since $\nabla^2 U_2(x,y) = 0$, the function $U_2(x,y)$ is the basis for a possible potential function in charge free space. Its equipotential lines and a potential surface are illustrated in Figure 2.13. The hyperbolic equipotential surfaces—or their cylindrical approximations—can be arbitrarily set on a circle of radius r_0 so that a potential difference between poles pairs of $2r_0^2\Phi_0$ will give the potential

$$\Phi = \Phi_0\left(x^2 - y^2\right), \tag{2.22}$$

as already discussed.

**Decapole**   The function z^n for $n=5$ is evaluated to obtain:

$$\begin{aligned} U_5(x,y) &= x^5 - 10x^3y^2 + 5xy^4 \\ V_5(x,y) &= 5x^4y - 10x^2y^3 + y^5 \, . \end{aligned} \tag{2.23}$$

The hyperbolic equipotential surfaces—or their cylindrical approximations—are set on a circle of radius r_0 and a voltage between pole pairs of $2r_0^5\Phi_0$ is chosen so that the potential obtained from the basis $U_5(x,y)$ is
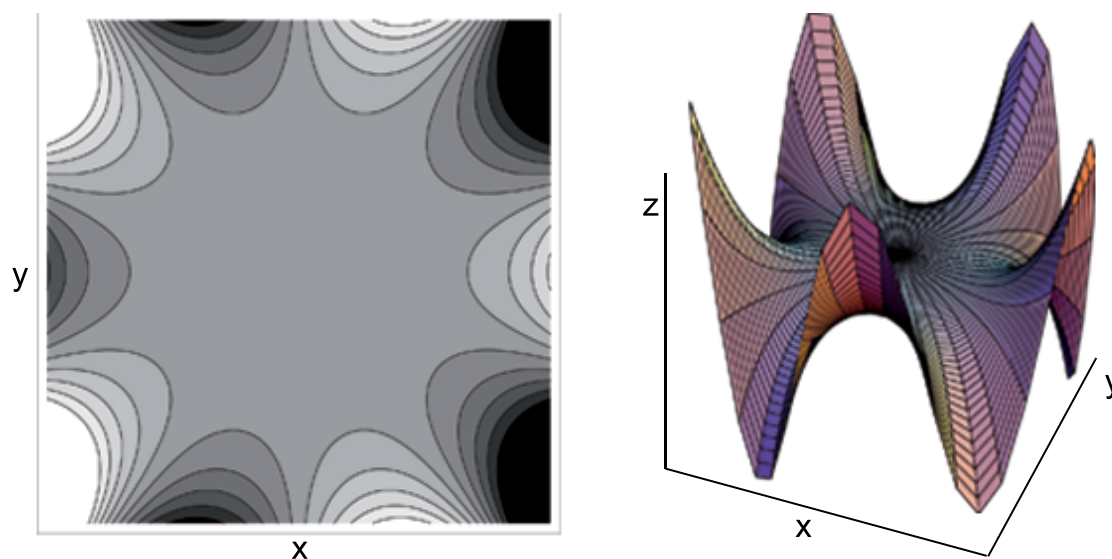
$$\Phi = \Phi_0\left(x^5 - 10x^3y^2 + 5xy^4\right). \tag{2.24}$$

Its equipotential lines and a potential surface are illustrated in Figure 2.14.
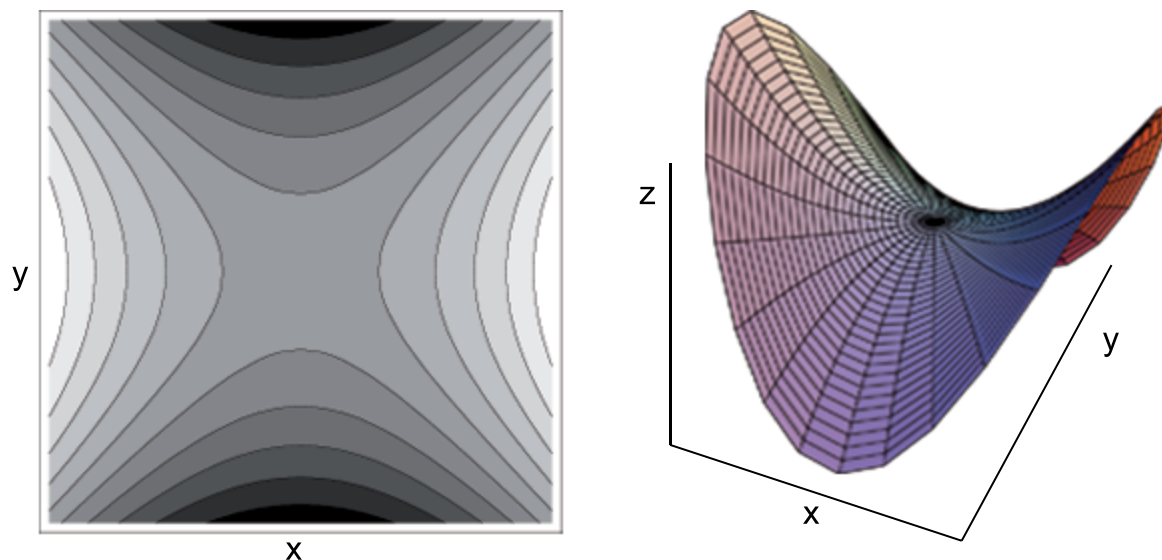
Figure 2.13: Quadrupole geometry. Left: A two-dimensional plot of the equipotential lines, where white corresponds to the potential $+\Phi_0$ and black to $-\Phi_0$. Right: A three-dimensional plot of the potential surface.

Figure 2.14: Decapole geometry. Left: A two-dimensional plot of the equipotential lines, where white corresponds to the potential $+\Phi_0$ and black to $-\Phi_0$. Right: A three-dimensional plot of the potential surface.

Hexadecapole The function z^n for n=8 is evaluated to obtain:

$$
\begin{aligned}
U_8(x,y) &= x^8 - 28x^6y^2 + 70x^4y^4 - 28x^2y^6 + y^8 \\
V_8(x,y) &= 8x^7y - 56x^5y^3 + 56x^3y^5 - 8xy^7 \; .
\end{aligned}
\tag{2.25}
$$

The hyperbolic equipotential surfaces—or their cylindrical approximations—are set on a circle of radius r_0 and a voltage between pole pairs of $2r_0^8\Phi_0$ is chosen so that the potential obtained from the basis $U_8(x, y)$ is

$$\Phi = \Phi_0\left(x^8 - 28x^6y^2 + 70x^4y^4 - 28x^2y^6 + y^8\right).\qquad(2.26)$$

Its equipotential lines and a potential surface are illustrated in Figure 2.15.
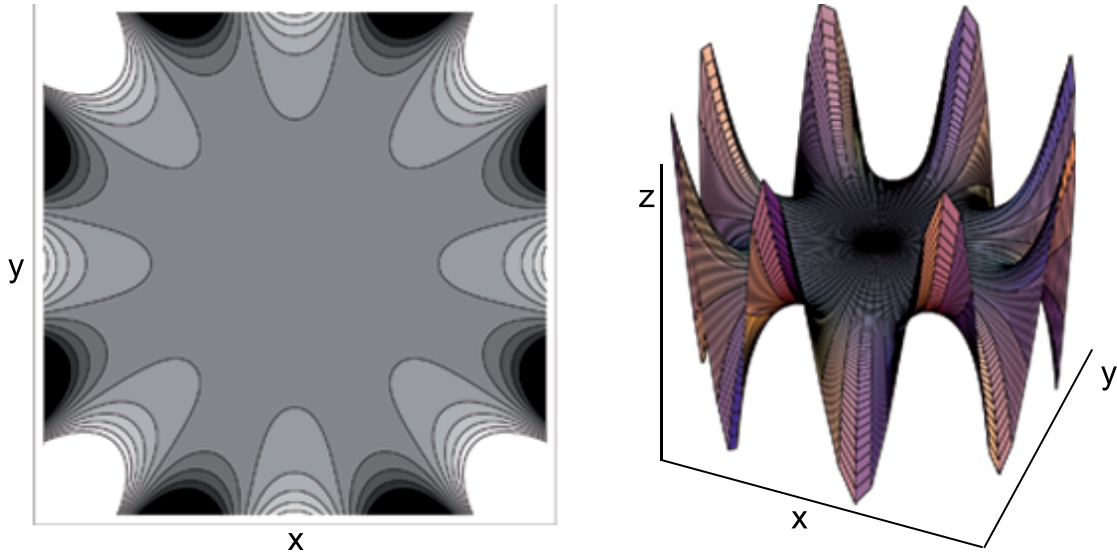
Figure 2.15: Hexadecapole geometry. Left: A two-dimensional plot of the equipotential lines, where white corresponds to the potential $+\Phi_0$ and black to $-\Phi_0$. Right: A three-dimensional plot of the potential surface.

Equations of Motion

Within the approximation of infinitely long conductors whose shape does not vary with z, the equation of motion in the z-direction is trivial and can be integrated directly

$$z = v_{z_0}t + z_0\,.$$

As anticipated in the quadrupole example, by applying an oscillating potential on the rods it is possible to obtain a confining field inside the trap. Therefore, a time-dependent term must be introduced in the potential formulas derived above. Hence, the general form for the potential is

$$\Phi = \cos(\omega t)\,\Phi_0\,U_n(x, y)\,.\qquad(2.27)$$

The force acting on an ion according to Lorentz's law (2.9) is

$$\boldsymbol{F} = -e\boldsymbol{\nabla}\Phi$$

or, using (2.27),

$$\boldsymbol{F} = -e\cos(\omega t)\,\Phi_0\,\boldsymbol{\nabla}U_n(x,y)\,. \tag{2.28}$$

In the case of a quadrupole, this leads to the two decoupled equations of motion

$$m\ddot{x} + 2e\Phi_0\cos(\omega t)x = 0 \tag{2.29}$$

$$m\ddot{y} - 2e\Phi_0\cos(\omega t)y = 0\,. \tag{2.30}$$

The two equations are equivalent since the plus or minus sign simply translates in a phase difference in the cosine argument. These equations are known as Mathieu's equations and their solutions are known as Mathieu's functions. It is difficult to visualize the space of solutions but the analysis of some special cases can help in understanding some properties of the solutions. In figure 2.16 eight solutions are plotted. Assuming an ion with a mass of 100 amu and a voltage amplitude of 50 V applied on electrodes that are separated by 1 cm, the plots show $x(t)$ for different values of ω. The ion moves with large and slow oscillations around $x = 0$ for $\omega = 10^6$ rad/s. The oscillation amplitude becomes smaller and its frequency increases with decreasing ω. Since it is desirable for many applications to keep ions close to the center of the trap $\omega = 2\cdot 10^5$ rad/s turns out to be an appropriate value for the present simulation. For even lower values of ω, $x(t)$ becomes instable and the oscillation amplitude diverges.
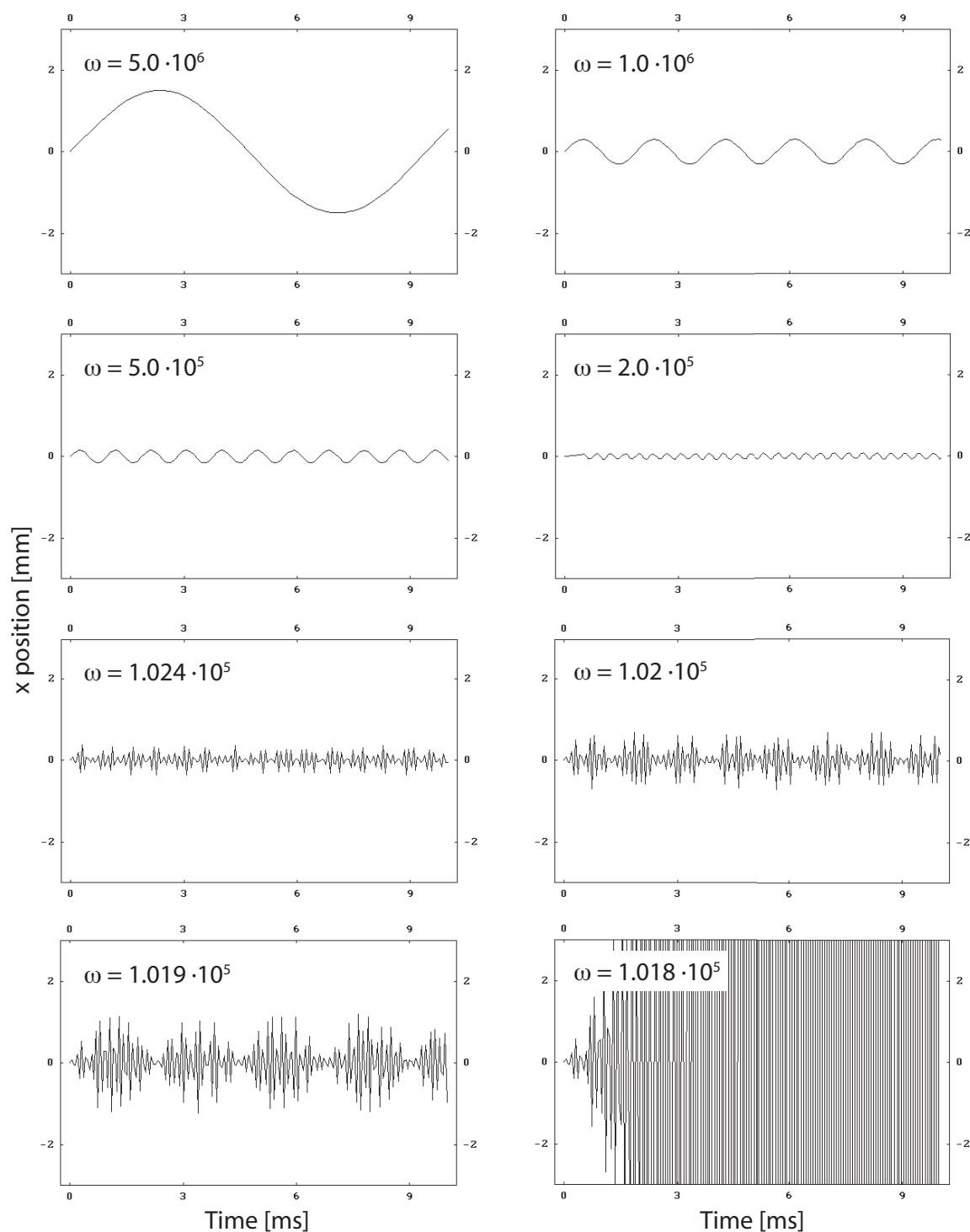
Figure 2.16: Different trajectories $x(t)$ for an ion of mass 100 amu in a quadrupole, in dependence of the applied frequency ω. The applied potential amplitude is 50 V and the distance between opposite electrodes is 1 cm.